Chemical Science

ROYAL SOCIETY OF CHEMISTRY

EDGE ARTICLE

View Article Online
View Journal | View Issue

Cite this: *Chem. Sci.*, 2025, **16**, 17470

All publication charges for this article have been paid for by the Royal Society of Chemistry

Received 8th July 2025
Accepted 25th August 2025

DOI: 10.1039/d5sc05061h

rsc.li/chemical-science

Regioselective construction of two isomeric BN-fused aromatic frameworks enabling the synthesis of ultralong room-temperature phosphorescence materials

Qiang Feng,†[a] Junxiong Yao,†[ab] Qianxin Wu,[a] Yang Qiu,[a] Zicheng Wang,[a] Xia Wang,[a] Weilin Chen,[a] Sibo Tong,[a] Xiaohua Cao,[a] Jianqi Sun,[a] Qianqian Ye,[a] Jianhua Liu,*[a] Dianyuan Wang,*[a] Jianguo Wang*[b] and Huanan Huang*[a]

BN-fused aromatic compounds have garnered significant attention due to their unique electronic structures and exceptional photophysical properties, positioning them as highly promising candidates for applications in organic optoelectronics. However, the regioselective synthesis of BN isomers remains a formidable challenge, primarily stemming from the difficulty in precisely controlling reaction sites, limiting structural diversity and property tunability. Herein, we propose a regioselective synthetic strategy that employs 2,1-BN-naphthalene derivatives, wherein selective activation of N–H and C–H bonds is achieved in conjunction with *ortho*-halogenated phenylboronic acids. Under uniform reaction conditions, two distinct boron–nitrogen fused ring isomers were successfully synthesized. A computational analysis of C–X bond dissociation energies indicates that the observed regioselectivity is most likely governed by the interplay of halogen electronegativity, atomic radius, and bond dissociation energy parameters. Interestingly, the two isomers exhibit markedly distinct room-temperature phosphorescence (RTP) in polyvinyl alcohol (PVA). Specifically, **3a@PVA** demonstrates ultralong RTP characteristics, featuring an exceptionally long phosphorescence lifetime of up to 2388.2 ms and an afterglow persisting for more than 30 seconds, significantly longer than the 286.1 ms observed for **4a@PVA**. Theoretical investigations reveal that **3a** possesses a higher spin–orbit coupling constant and more intersystem crossing channels than **4a**. Additionally, the dual-sided fixation of the **3a@PVA** system imposes significant constraints on intramolecular motions, effectively suppressing non-radiative decay pathways, which accounts for its distinct afterglow behaviors. These divergent photophysical characteristics significantly enhance their potential applications in advanced anti-counterfeiting technologies. This work not only establishes a versatile synthetic strategy for the regioselective construction of BN-fused isomers but also provides fundamental insights into the rational design of BN-incorporating organic RTP systems.

Introduction

Boron–nitrogen (BN) aromatic compounds have garnered significant attention in recent years owing to their distinctive physicochemical properties and have broad applications in organic synthesis, materials science, and related interdisciplinary fields.[1–5] In contrast to conventional all-carbon aromatics, BN aromatics feature isoelectronic substitution of C=C units with B–N units, which perturbs the π-conjugated system and endows the molecules with distinct electronic characteristics, enhanced thermal stability, and tuneable optical properties.[6–8] These features make BN aromatics highly promising for applications in optoelectronic devices,[9–13] chemical sensing,[14–20] and pharmaceutical design[21–24] (Fig. 1A). Despite their potential, synthesizing BN aromatics remains a formidable challenge. Traditional approaches often involve electrophilic borylation under harsh conditions or multistep protocols, which suffer from low efficiency, poor atom economy, and limited structural diversity.[25,26] Consequently, the development of efficient, selective, and broadly applicable synthetic strategies is essential not only for advancing BN chemistry but also for realizing their potential in diverse application domains.

[a]*College of Chemistry and Chemical Engineering, Jiangxi Province Engineering Research Center of Ecological Chemical Industry, Jiujiang University, Jiujiang 332005, China. E-mail: huanan200890@163.com*

[b]*College of Chemistry and Chemical Engineering, College of Green Chemistry and Environment, Institutes of Biomedical Sciences, Inner Mongolia Key Laboratory of Synthesis and Application of Organic Functional Molecules, Inner Mongolia University, Hohhot 010021, P. R. China. E-mail: wangjg@iccas.ac.cn*

† These authors contributed equally.

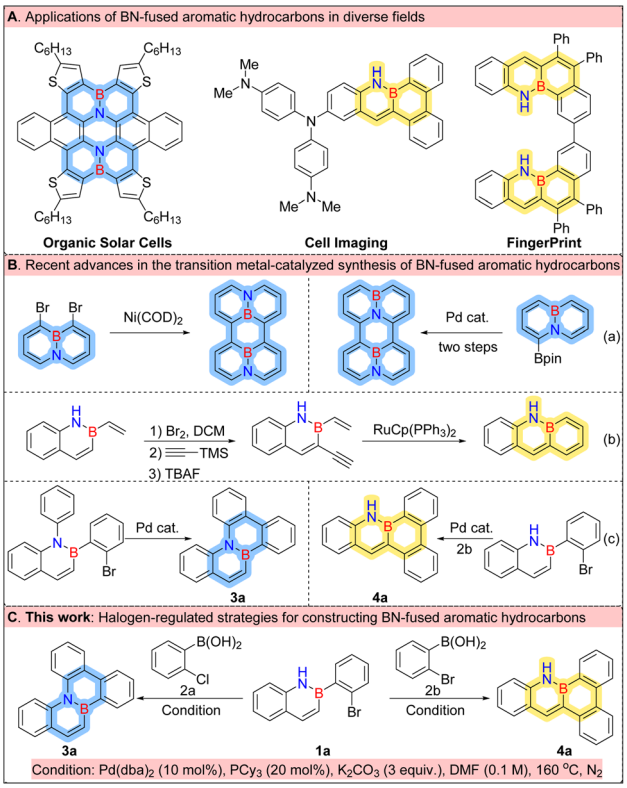

Fig. 1 (A) Applications of BN-fused aromatic hydrocarbons in diverse fields. (B) Transition metal-catalyzed synthesis of BN-fused aromatic compounds. (C) Halogen-regulated strategies for constructing BN-fused aromatic hydrocarbons.

Recent advances in transition metal-catalysed coupling reactions and C–H activation strategies have significantly expanded the range of tools available for constructing boron–nitrogen (BN)-fused polycyclic frameworks. Notably, Cui and his colleagues pioneered a tandem insertion/C–H activation strategy for synthesising boron–nitrogen (BN)-embedded tetraphene derivatives.[27] In parallel, palladium-catalysed methodologies reported by Liu[28] and Park[29] have facilitated the efficient assembly of diverse BN aromatic scaffolds. Nickel-catalysed systems developed by Wang[7] and Song[30] have also demonstrated excellent reactivity and functional group tolerance (Fig. 1B(a)). Furthermore, catalytic systems based on rhodium,[31–33] ruthenium,[34,35] and gold[36–38] have shown promising potential in related transformations (Fig. 1B(b)). Our group is dedicated to constructing boron–nitrogen (BN) aromatic frameworks. We have developed an efficient C–H activation protocol utilising diverse substrates and optimised reaction conditions to successfully synthesise compounds **3a** (ref. 17) and **4a** (ref. 39) (Fig. 1B(c)). However, this strategy imposes stringent requirements on the substrate structure. Despite these achievements, challenges remain, particularly with regard to site selectivity, which is often compromised by the intrinsic electronic and steric properties of the substrates. Therefore, integrating transition metal catalysis with rational substrate design to achieve regioselective functionalisation is a key way of streamlining the synthesis of structurally diverse BN-containing aromatics.

Herein, we present a halogen-regulated synthetic approach that exploits the differential reactivity patterns of aryl halides to govern the sequential order of bond-forming processes. Compound **1a** was selected as the precursor core, featuring two distinct types of reactive hydrogen sites-C(3)–H and N–H. The reactivity hierarchy of these sites is governed by the intrinsic properties of the aryl halide substrate, thereby facilitating selective pathway modulation. As anticipated, this synthetic strategy successfully afforded a pair of BN-fused aromatic isomers, namely compounds **3** and **4**. Moreover, photophysical analyses demonstrated that both compounds exhibit RTP phenomena when incorporated into a PVA matrix. However, the two isomers embedded in PVA exhibit marked differences in RTP lifetime and emission color. Notably, the **3a@PVA** system exhibits an exceptionally long phosphorescence lifetime of 2388.2 ms and visible afterglow persistence for up to over 30 seconds under ambient conditions. Additionally, patterned emissive images with well-defined motifs were successfully obtained, underscoring the potential of this system for applications in anti-counterfeiting and information display technologies. This work provides a novel synthetic approach for designing BN-fused aromatic compounds with excellent properties, providing a valuable opportunity to explore the relationship between the structure and RTP properties, which is of considerable importance for advancing the development of boron–nitrogen functional molecules with enhanced performance.

Results and discussion

Our investigation initially centered on the coupling reaction between 2,1-BN naphthalene (**1a**) and *ortho*-chlorophenylboronic acid (**2a**), under a variety of conditions employing different palladium catalysts, phosphine ligands, and bases (Table 1). The reaction was first conducted in *N*,*N*-dimethylformamide (DMF) at 160 °C using 10 mol% $Pd(OAc)_2$, 20 mol% PCy_3, and 3 equivalents of Na_2CO_3 over 24 hours, affording the desired product **3a** in 18% isolated yield (Table 1, entry 1). Encouraged by this initial result, we performed a systematic optimization of the catalytic system. Screening of palladium sources revealed that $Pd(dba)_2$ significantly improved the yield to 54% (entry 2), outperforming other tested catalysts such as $Pd(PPh_3)_2Cl_2$ and $Pd(dppf)Cl_2$. Subsequent ligand screening included sterically demanding X-phos (entry 5), less hindered PPh_3 (entry 6), and bidentate dppf (entry 7), none of which led to further yield enhancement. Evaluation of bases revealed that replacing Na_2CO_3 with K_2CO_3 markedly improved the yield of **3a** to 85% (entry 8), while weaker bases such as $NaHCO_3$ gave lower yields (63%, entry 9). Stronger bases like Cs_2CO_3 and NaOAc resulted in diminished efficiency, attributable to decomposition of the sensitive BN substrate under overly basic conditions (entries 10 and 11). To further explore the halogen-regulated pathway, 2-chlorophenylboronic acid (**2a**) was replaced with its bromo analogue **2b** under the optimized reaction conditions. Interestingly, this modification

Table 1 Optimization conditions[a]

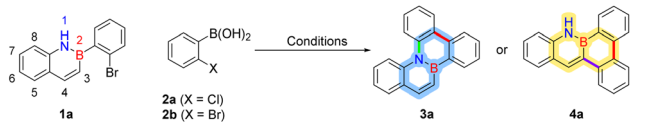

Entries	Cat.	Ligand	Base	Yield[b]
1	$Pd(OAc)_2$	PCy_3	Na_2CO_3	18%
2	$Pd(dba)_2$	PCy_3	Na_2CO_3	54%
3	$Pd(PPh_3)Cl_2$	PCy_3	Na_2CO_3	13%
4	$Pd(dppf)Cl_2$	PCy_3	Na_2CO_3	15%
5	$Pd(dba)_2$	X-phos	Na_2CO_3	48%
6	$Pd(dba)_2$	PPh_3	Na_2CO_3	68%
7	$Pd(dba)_2$	dppf	Na_2CO_3	46%
8	$Pd(dba)_2$	PCy_3	K_2CO_3	85%
9	$Pd(dba)_2$	PCy_3	$NaHCO_3$	63%
10	$Pd(dba)_2$	PCy_3	Cs_2CO_3	14%
11	$Pd(dba)_2$	PCy_3	NaOAc	23%
12[c]	$Pd(dba)_2$	PCy_3	K_2CO_3	53%

[a] Reaction conditions: 1a (1.0 equiv., 0.2 mmol), 2a (1.0 equiv., 0.2 mmol), Pd-cat. (10 mol%), ligand (20 mol%), base (3.0 equiv., 0.6 mmol), DMF (1.0 mL), 160 °C, 24 h, N_2 atmosphere. [b] Isolated yield. [c] 1a (1.0 equiv., 0.2 mmol) and 2b (1.0 equiv., 0.2 mmol) as substrates.

led to the formation of a distinct BN-fused product, **4a**, in 53% isolated yield, thus demonstrating the impact of halogen substitution on the reaction trajectory and product outcome.

Under the optimized conditions, we successfully synthesized a series of BN-fused aromatic compounds, as summarized in Table 2. The coupling of various *ortho*-chlorophenylboronic acids with **1a** proceeded smoothly, affording products **3a**, **3b**, and **3d** in moderate to good yields. However, when an electron-deficient arylboronic acid was employed, the yield of **3c** dropped significantly to 23%, likely as a result of the diminished nucleophilicity of the boronic acid.[40] Notably, substitution of compound **1** with electron-withdrawing fluorine atoms had little effect on the reaction efficiency: target compounds **3e** and **3f** were obtained in satisfactory yields, highlighting the robustness of the protocol toward electronic variations in the BN framework. We next turned our attention to the reactivity of *ortho*-bromophenylboronic acid under the same conditions. The corresponding coupling with **1a** afforded product **4a** in 53% yield, confirming the viability of the C–H activation pathway. In contrast, employing thiophene boronic acid as the coupling partner resulted in a reduced yield of 15% for **4b**, likely due to the strong coordination of the sulfur heteroatom with the catalyst, which hampers C–H activation efficiency and promotes competing side reactions in the electron-deficient heterocyclic scaffold.[41] Similarly, the coupling of an electron-deficient variant of **1a** afforded product **4c** in only 30% yield, likely attributable to diminished reactivity at the C(3) position of the electron-poor BN scaffold, arising from the electron-withdrawing group reducing the arene's electron density and thereby impeding catalyst coordination and C–H activation efficiency.[42] These results underscore the critical influence of electronic effects on both boronic acid and BN substrate reactivity in these halogen-regulated transformations.

Based on our experimental observations, we propose a plausible reaction mechanism for this halogen-regulated transformation (Fig. 2). The initial step involves a Suzuki–Miyaura coupling of **1a** with either **2a** or **2b**, affording intermediates **2a-I** and **2b-I**, respectively. The subsequent divergence in the reaction pathway is governed by the nature of the carbon–halogen bond. Intermediate **2a-I**, bearing a less reactive C–Cl bond, preferentially undergoes Buchwald–Hartwig amination *via* N–H bond activation to deliver product **3a**. In contrast, the more reactive C–Br bond in intermediate **2b-I** facilitates a C–H activation pathway, resulting in the formation of **4a**. This mechanistic rationale accounts for the observed regioselectivity and highlights a direct correlation between halogen identity and pathway preference. To gain deeper insight into the origin of this selectivity, we conducted a comparative analysis of the transition states associated with N–H *versus* C–H activation in both intermediates. For substrate **2a**, several factors favor the N–H activation pathway: the high bond dissociation energy of the C–Cl bond (88 kJ mol^{-1}), the strong electronegativity of chlorine, and the favorable coordination ability of the nitrogen atom collectively stabilize the transition state.[43] Furthermore, the relatively low bond dissociation energy of the N–H bond (103 kJ mol^{-1}) lowers the activation barrier, rendering N–H cleavage kinetically accessible. In contrast, for substrate **2b**, the

Table 2 Substrate scope[a]

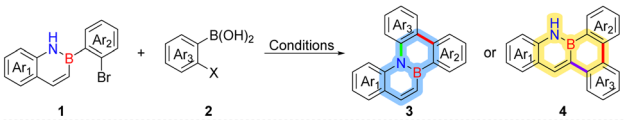

X = Cl, Ar_1 = Ph, Ar_2 = Ph, Ar_3 = Ph	3a, 85%
X = Cl, Ar_1 = Ph, Ar_2 = Ph, Ar_3 = 3-Me-Ph	3b, 75%
X = Cl, Ar_1 = Ph, Ar_2 = Ph, Ar_3 = 4-CHO-Ph	3c, 23%
X = Cl, Ar_1 = Ph, Ar_2 = Ph, Ar_3 = 2-Thiophene	3d, 55%
X = Cl, Ar_1 = Ph, Ar_2 = 4-F-Ph, Ar_3 = Ph	3e, 50%
X = Cl, Ar_1 = 4-F-Ph, Ar_2 = 4-F-Ph, Ar_3 = Ph	3f, 63%
X = Br, Ar_1 = Ph, Ar_2 = Ph, Ar_3 = Ph	4a, 53%
X = Br, Ar_1 = Ph, Ar_2 = Ph, Ar_3 = 3-Thiophene	4b, 15%
X = Br, Ar_1 = 4-F-Ph, Ar_2 = Ph, Ar_3 = Ph	4c, 30%

[a] Conditions: **1** (1.0 equiv., 0.2 mmol), **2** (1.0 equiv., 0.2 mmol), $Pd(dba)_2$ (10 mol%), PCy_3 (20 mol%), K_2CO_3 (3 equiv., 0.6 mmol), DMF (1 mL), 160 °C, 12 h, N_2 atmosphere.

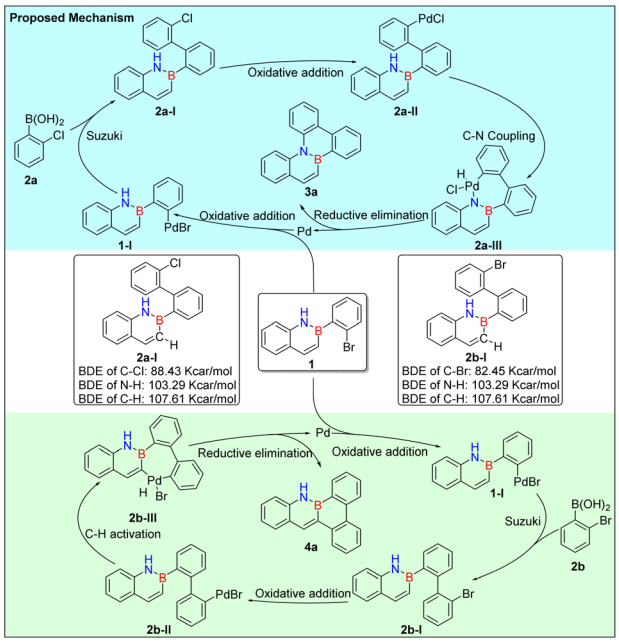

Fig. 2 Proposed mechanism for the synthesis of compounds **3a** and **4a**.

reaction is biased toward C–H activation. This preference is attributed to the lower bond dissociation energy of the C–Br bond (82.1 kJ mol^{-1}) and the larger atomic radius and weaker electronegativity of bromine. These features reduce steric hindrance and enhance the electrophilicity of the adjacent C–H bond, thereby facilitating its activation by the transition metal catalyst. Collectively, these results underscore the critical role of halogen identity in dictating divergent bond activation pathways and product selectivity in BN-fused aromatic ring construction.

Following the successful synthesis of BN-fused aromatic compounds, the UV-vis absorption, fluorescence emission and quantum yield of compounds **3** and **4** were systematically investigated (Fig. 3 and Table 3). Compounds **3a–3f** exhibited absorption maxima in the range of 335–357 nm (Fig. 3a). Notably, compound **3c** showed a significant redshift relative to **3a**, which can be attributed to the enhanced π-conjugation induced by the aldehyde group (C=O). In contrast, compounds **4a–4c** displayed multiple absorption bands, with intense peaks appearing between 376 and 383 nm (Fig. 3d)—significantly redshifted compared to their counterparts in series 3—highlighting the critical influence of the position of BN units within the molecular framework on the electronic structure and absorption characteristics. Photoluminescence studies revealed that the two series of isomers exhibit emissive behaviour in solution and the solid state. In dichloromethane, compounds **3a–3f** displayed fluorescence emission bands ranging from 393 to 430 nm (Fig. 3b). Among them, **3d** exhibited a pronounced redshift (λ_{em} = 430 nm), likely due to the introduction of a sulfur atom, which enhances π-conjugation—a phenomenon consistent with previously reported observations.[44,45] However, compounds **4a–4c** exhibited negligible red-shifted emission wavelengths, spanning the range of 404–409 nm (Fig. 3e). Notably, these compounds also exhibit solid-state fluorescence, with emission wavelengths red-shifted relative to their solution-state counterparts. In the case of **3**-series compounds, incorporating sulfur atoms or aldehyde groups into the molecular framework results in a red shift in solid-state emission compared to **3a** (Fig. 3c). Conversely, the **4**-series compounds exhibit negligible variations in their solid-state fluorescence profiles. These findings highlight the potential of these compounds for applications in solid-state optoelectronic materials.

Furthermore, the photoluminescence quantum yields (Φ) were found to be highly sensitive to the intrinsic properties of substituents (Table 3). For instance, compound **3a** displayed an extremely low Φ of 0.19% in solution, indicative of its almost non-emissive nature, while the introduction of either an aldehyde group[46] (**3c**) or a sulfur-containing[47] moiety (**3d**) completely quenched the emission, leading to quantum yields approaching zero. In contrast, compounds **4a** and **4c** exhibited remarkably high quantum yields of 69.80% and 67.37% in solution states, respectively, while the presence of a sulfur-containing heterocycle in **4b** resulted in a lower quantum yield of 20.79%. In the solid state, the quantum yields were found to decrease compared to their solution-state counterparts. Compound **4a** exhibited a quantum yield of 49.30%, while those of **4b** and **4c** decreased to 0% and 16.66%, respectively, upon the incorporation of sulfur or fluorine atoms. Collectively, these results underscore the pivotal role of BN unit positioning and substituent effects in modulating the photophysical behaviour of these systems, offering valuable guidance for the rational design of high-performance organic emitters.

Organic Room-Temperature Phosphorescence (ORTP) materials[48] have attracted growing interest attributable to their potential applications in bioimaging,[49–52] sensing,[53,54] and optical displays.[55–57] Their favorable features—including low cytotoxicity, structural tunability, long-lived emission, high signal-to-noise ratios, minimal background fluorescence, and strong resistance to light scattering—make them particularly appealing for real-world applications. However, despite these advantages, ORTP materials often suffer from inherent drawbacks such as poor mechanical properties, limited processability, and high sensitivity to oxygen and moisture, which collectively hinder their integration into practical devices and large-scale applications. These challenges necessitate the development of strategies to improve their structural robustness, environmental stability, and fabrication compatibility. To address these limitations, incorporating ORTP luminophores into appropriate host matrices has proven to be an effective strategy for enhancing their mechanical strength, processability, and environmental stability. In particular, polymeric matrices can not only provide structural support but also create confined microenvironments that suppress nonradiative decay pathways and protect triplet excitons from quenching by oxygen and moisture. Accordingly, two representative BN-fused aromatic compounds, **3a** and **4a**, were selected as model systems to investigate their RTP behavior in different physical

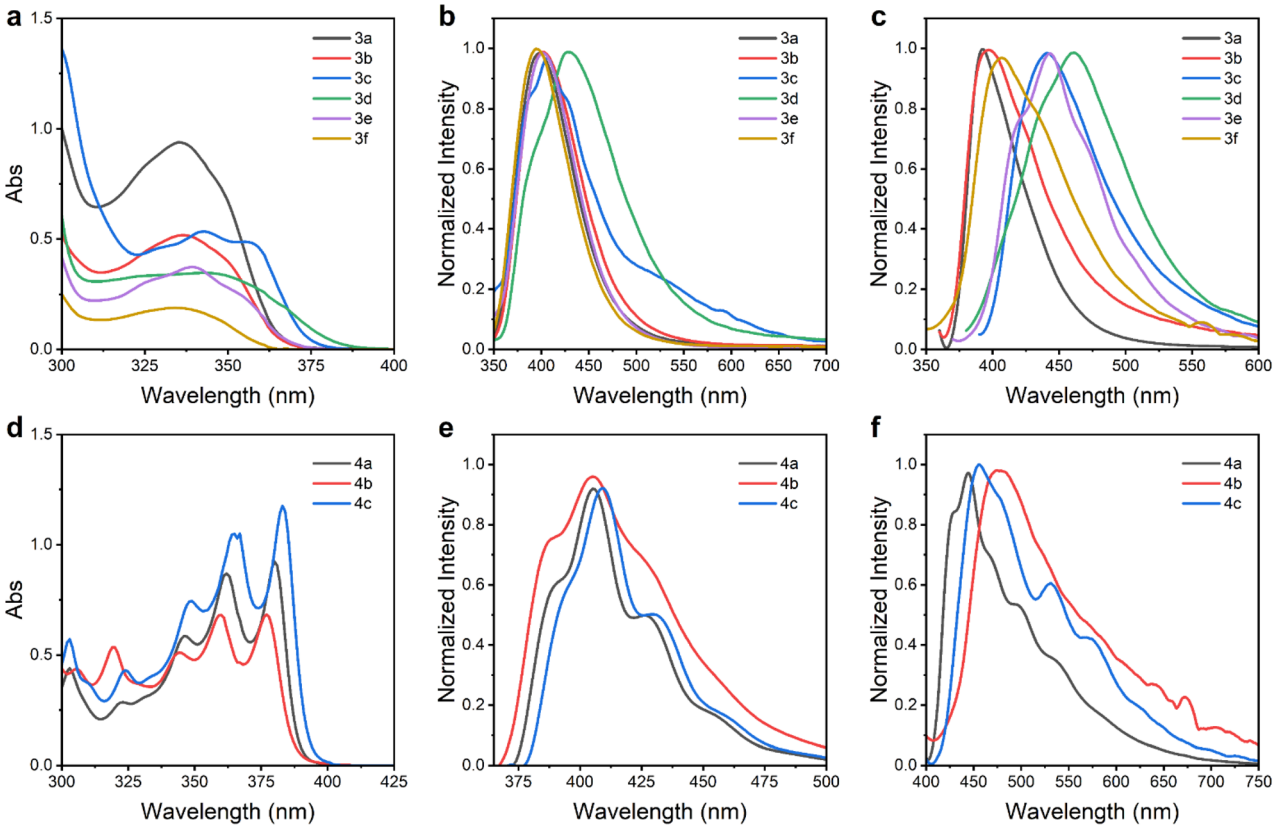

Fig. 3 (a) The UV-vis spectra of **3a–3f** in DCM (concentration = 10^{-5} M). (b) Fluorescence spectra of **3a–3f** in DCM. (c) Solid-state fluorescence spectra of **3a–3f**. (d) The UV-vis spectra of **4a–4c** in DCM (concentration = 10^{-5} M). (e) Fluorescence spectra of **4a–4c** in DCM. (f) Solid-state fluorescence spectra of **4a–4c**.

states and various polymer matrices, thereby validating the role of polymer hosts in modulating their emission properties.

Systematic investigations revealed that, under ambient conditions, neither compound exhibits RTP in solution (Fig. S1 and S4). Moreover, compound **4a** shows no RTP in both the solid state (Fig. S5) and crystalline states (Fig. S6), whereas **3a** displays only a very weak phosphorescence signal in these states (Fig. S2 and S3). Furthermore, the phosphorescence lifetimes of both compounds could not be detected at room temperature in solution, solid states, or crystalline states, further confirming that RTP behaviours were not observable for **3a** and **4a** under these conditions. Previous studies have revealed that **3a** adopts a non-planar twisted conformation[17] (Fig. S16). Based on this structural feature, we hypothesized that incorporating **3a** into a polymer matrix could effectively restrict molecular vibrations,[58] thereby suppressing non-radiative decay pathways and enhancing RTP performance. Furthermore, both compounds contain polar B–N bonds that provide a robust structural basis

Table 3 Photophysical properties of **3a–3f** and **4a–4c** in dichloromethane and in the solid state

Compound	λ_{max}, abs[a] [nm]	λ_{max}, em[a] [nm]	Stokes shifts [cm^{-1}] in DCM	Φ_F[b] [%]	λ_{max}, em[c] [nm]	Solid state Stokes shifts [cm^{-1}]	Φ_F[b,c] [%]
3a	335	396	4598	0.19[d]	392	4340	3.3[d]
3b	337	402	4798	8.58	397	4485	4.65
3c	357	408	3501	0	441	5335	0.18
3d	347	430	5563	0	460	7079	0
3e	339	402	4623	7.50	442	6874	0.28
3f	335	394	4470	8.32	405	5159	0.22
4a	380	404	1563	69.80[d]	443	3741	49.30[d]
4b	376	404	1843	20.79	476	5587	0
4c	383	409	1660	67.37	455	4132	16.66

[a] All experiments were performed in DCM solution at 10^{-5} M. [b] Absolute quantum yield determined using a calibrated integrating sphere system within ±3%; the absolute quantum yield was measured in DCM at room temperature. [c] All experiments were performed in the solid state. [d] The relevant data were reported previously.[17,39]

for interaction with polymer matrices. The highly electronegative nitrogen atoms can form hydrogen bonds[59] with hydroxyl groups, while the electron-deficient boron centers can coordinate with oxygen atoms *via* B–O bonds.[60,61] Based on these considerations, polyvinyl alcohol (PVA), poly(methyl methacrylate) (PMMA), and polyvinylpyrrolidone (PVP) were selected as host matrices to evaluate the RTP properties of the two compounds at 297 K. The results demonstrate that both compounds exhibit RTP in all three matrices, albeit with significant differences in phosphorescence lifetimes. Specifically, compound **4a** shows lifetimes of 286.1 ms, 408.8 ms, and 516.27 ms in PVA (Fig. S10), PMMA (Fig. S11), and PVP (Fig. S12), respectively, while compound **3a** exhibits lifetimes of 2388.2 ms (Fig. S7), 8.82 ms (Fig. S8), and 669.96 ms (Fig. S9) in the corresponding matrices. Considering the overall RTP lifetimes and stability, PVA was chosen as the polymer matrix for further detailed investigations. The resulting films exhibited visually discernible blue (**3a@PVA**) and yellow (**4a@PVA**) afterglow emissions that persisted for several seconds under ambient conditions. Delayed emission spectra (Fig. 4a, e and Table 4) revealed marked red shifts relative to their prompt fluorescence, corroborating the dual-emissive nature of these systems—featuring both fluorescence and ultralong phosphorescence components. To further optimize and evaluate their performance, we systematically investigated the influence of doping concentration on RTP intensity. As shown in Fig. 4b and f, **3a@PVA** exhibited maximum phosphorescence intensity at a doping level of 0.3 mg mL^{-1}, whereas higher concentrations led to a gradual quenching of emission. A similar trend was observed for **4a@PVA**. This concentration-dependent quenching is likely due to enhanced intermolecular interactions at elevated doping levels,[62] which facilitate non-radiative deactivation pathways and suppress phosphorescence. In addition to concentration effects, temperature was found to play a critical role in modulating RTP behaviours. Time-resolved photoluminescence decay measurements were carried out across a range of temperatures, revealing that the phosphorescence lifetimes of both films decreased progressively with rising temperature (Fig. S13–S15). Notably, under ambient conditions, **3a@PVA** exhibited an exceptional phosphorescence lifetime of 2388.2 ms (Fig. 4c), significantly longer than the 286.1 ms lifetime recorded for **4a@PVA** (Fig. 4g). These findings highlight the profound influence of BN unit positioning on the RTP performance of the materials. The pronounced differences in their photoluminescent behaviors thereby prompted us to further elucidate the underlying mechanisms.

Elucidating the light-emission process is essential for understanding the fundamental mechanisms underlying photoluminescence. The interplay between intersystem crossing (ISC) and spin–orbit coupling (SOC) plays a pivotal role in the generation of RTP. To qualitatively analyze the energy levels of singlet and triplet states, TD-DFT calculations were performed to map the singlet and triplet energy levels and evaluate potential ISC pathways. Efficient singlet-to-triplet ($S_1 \rightarrow Tn$) transition pathways were systematically identified by applying a stringent energy gap criterion, specifically requiring the singlet-triplet energy splitting (ΔE_{ST}) to be within an absolute value of less than 0.3 eV.[63] Specifically, compound **3a** exhibits five effective ISC channels,[17] facilitating transitions from the singlet excited state S_1 to triplet states T_4, T_5, T_6, T_7 and T_8 (Fig. 4g). In contrast, **4a** features only two effective ISC pathways[17,39] (Fig. 4h). Further analysis of SOC values provided mechanistic insights into the distinct photophysical behaviours of the two compounds: **3a** displays SOC values ranging from 0.18 cm^{-1} to a maximum of 0.52 cm^{-1} (Fig. 4g and Table S1), which are significantly higher than those of **4a**, whose maximum SOC value reaches only 0.08 cm^{-1} (Fig. 4h and Table S2). These results indicate that, both in terms of the number of effective ISC channels and the SOC values, compound **3a** is more favourable for the generation of triplet excitons, which serves as a prerequisite for achieving RTP.[64]

It is of significant importance to elucidate the key factors responsible for the marked differences in RTP behaviour exhibited by **3a** and **4a**, despite their structural isomerism. To rationalise this phenomenon, a schematic illustration of the possible interactions between the compounds and the PVA matrix is proposed. It is evident that both **3a** and **4a** contain nitrogen (N) and boron (B) atoms, which facilitates the formation of hydrogen bonds[59] and B–O coordination interactions[60,61] with the PVA matrix. This effectively stabilises the system. However, a marked discrepancy in the spatial distribution of these interactions is evident between the two systems. In the **3a@PVA** system, the N and B atoms are positioned on opposite sides of the molecule, enabling bilateral anchoring within the PVA matrix (Fig. 5a). This spatial constraint significantly restricts intramolecular motions, effectively suppressing nonradiative decay pathways and thereby enhancing the RTP performance. In contrast, the **4a@PVA** system exhibits an asymmetric anchoring configuration, with both the N and B atoms located on the same side of the molecule (Fig. 5b). In this case, the N and B atoms preferentially interact with hydroxyl groups in the less sterically hindered regions of the PVA matrix through hydrogen bonding and B–O coordination, reaching a saturated coordination state. As a result, further interactions with PVA chains on the more sterically congested side are effectively impeded. Consequently, the molecular motions of **4a** are less constrained, resulting in enhanced nonradiative decay processes and significantly reduced emission efficiency. Moreover, the lower rigidity associated with this asymmetric structure facilitates vibrational relaxation, thereby promoting nonradiative energy dissipation. Experimental data further support our hypothesis. As shown in Table 4, the phosphorescence radiative decay rate (k_r^p) and nonradiative decay rate (k_{nr}^p) of **4a@PVA** are 37 times and 7.8 times higher, respectively, than those of **3a@PVA**. These findings indicate that the deactivation of triplet excitons in **3a@PVA** is significantly suppressed, directly contributing to its prolonged RTP lifetime.

To further assess the practical applicability of the synthesized materials in visual information display, we conducted patterning and phosphorescence decay imaging experiments using PVA-doped films of **3a** and **4a** (denoted as **3a@PVA** and **4a@PVA**, respectively). The **3a@PVA** film successfully reproduced a well-defined "deer" pattern (Fig. 5d and Video S2) as well as the Chinese characters for "Jiujiang University" (Fig. 5e

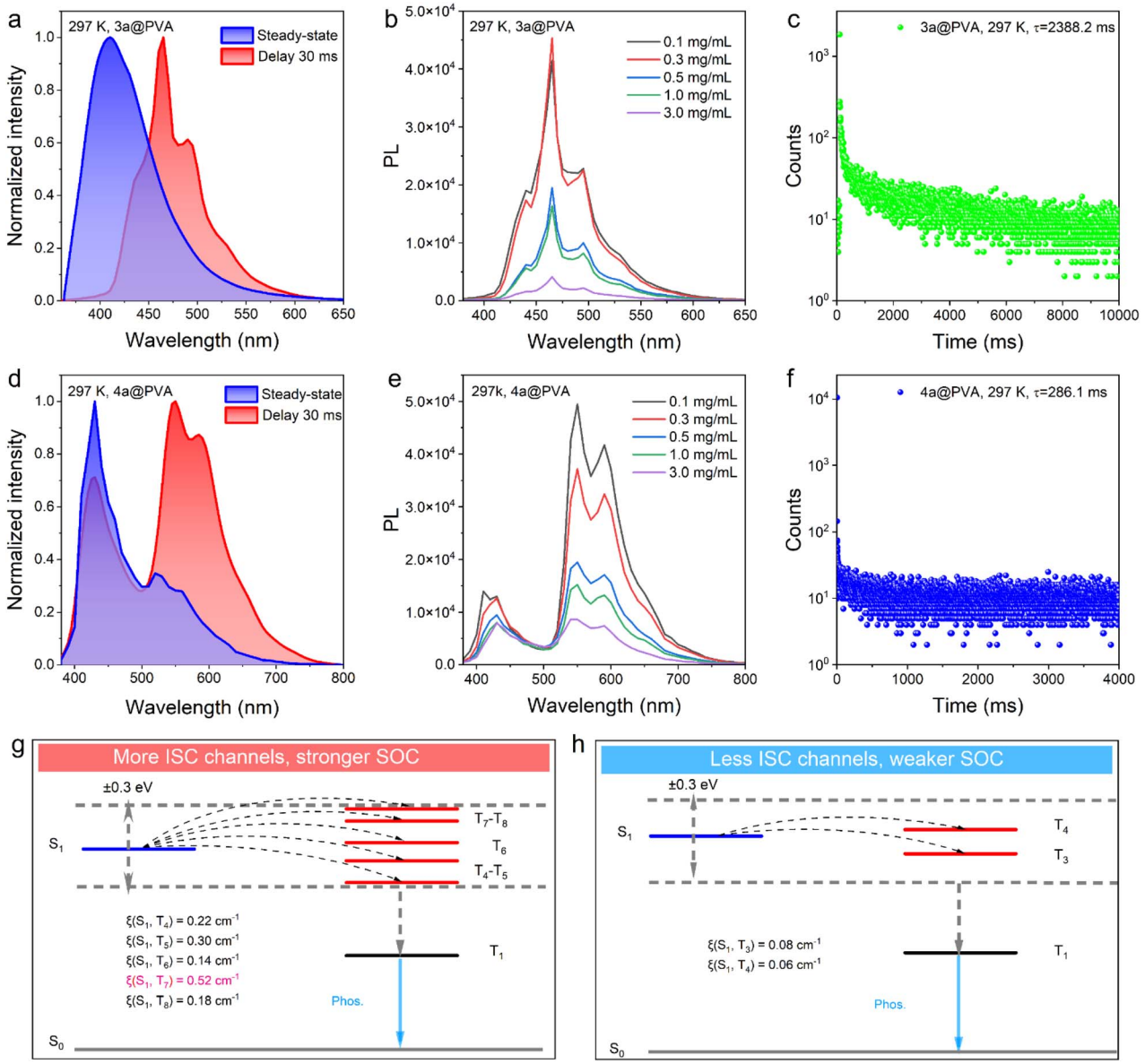

Fig. 4 Photophysical properties of PVA-doped films **3a@PVA** and **4a@PVA**. (a and d) Prompt and delayed PL spectra. (b and e) Doping concentration-dependent delayed PL spectra of films **3a@PVA** and **4a@PVA**. (c and f) Time-resolved phosphorescence decay curves. (g) Energy-level diagrams and possible ISC channels from excited singlet states (S_1) to excited triplet states (T_n) for **3a** (isolated). (h) Energy-level diagrams and possible ISC channels from excited singlet states (S_1) to excited triplet states (T_n) for **4a** (isolated).

and Video S3), both of which exhibited a vivid blue afterglow visible to the naked eye for up to 30 seconds. In contrast, the **4a@PVA** film enabled the generation of a similar "deer" pattern (Fig. 5c and Video S1), emitting a yellow afterglow with a markedly shorter lifetime of approximately 2 seconds. These results are in excellent agreement with the phosphorescence

Table 4 Photophysical data of the doped PVA films at room temperature[a]

Entries	λ_f [nm]	λ_p [nm]	Φ_t [%]	Φ_f [%]	Φ_p [%]	$\langle\tau\rangle_p$ [ms]	k_r^p [s^{-1}]	k_{nr}^p [s^{-1}]
3a@PVA	410	465	6.05	4.20	1.80	2388.2	0.0075	0.4110
4a@PVA	429	550	24.30	16.30	8.04	286.1	0.2800	3.2100

[a] λ_{ex} = 350 nm, delayed time = 30 ms. $\Phi_t = \Phi_f + \Phi_p$, $k_r^p = \Phi_p/\langle\tau\rangle_p$, and $k_{nr}^p = (1 - \Phi_p)/\langle\tau\rangle_p$. λ_f and λ_p are the emission maxima of fluorescence and phosphorescence of the crystals. Φ_t, Φ_f, and Φ_p are the quantum efficiencies of total emission, fluorescence, and phosphorescence of doped PVA, respectively.

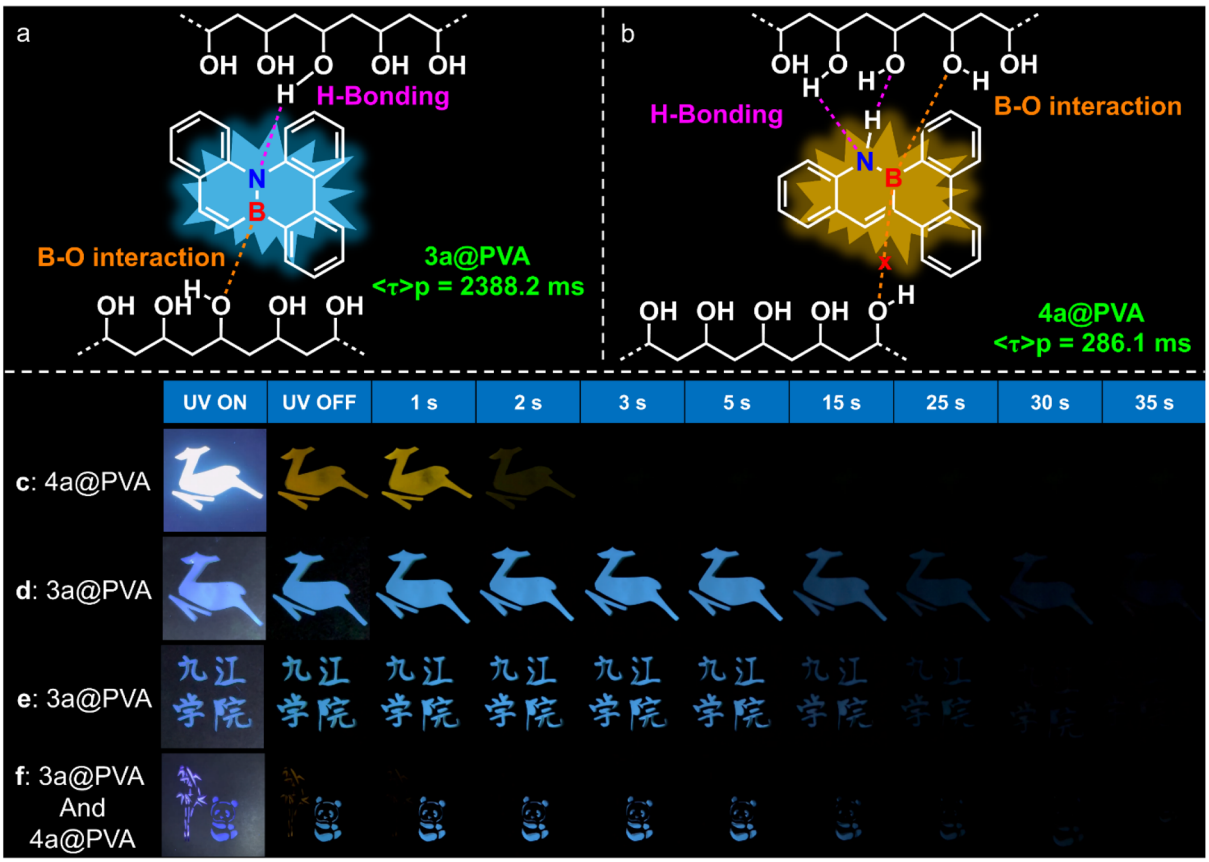

Fig. 5 (a and b) Possible schematic models of the interactions of **3a** and **4a** with PVA, respectively. (c–f) Potential applications of doping the PVA system in the fields of anti-counterfeiting and information encryption. (c) was excited under UV irradiation at a wavelength of 365 nm with a power of 10 W, while (d–f) were excited using a 10 W UV lamp at 265 nm.

lifetimes measured previously. To explore potential applications in optical anti-counterfeiting, we designed a composite pattern featuring "a panda under bamboo," in which the bamboo was rendered using **4a@PVA** and the panda using **3a@PVA** (Fig. 5f and Video S4). The pronounced differences in emission color and afterglow duration between the two films enabled the pattern to be temporally resolved upon cessation of excitation, thus demonstrating a robust time-gated luminescence encoding strategy. Taken together, these findings highlight the considerable promise of **3a@PVA** and **4a@PVA** as advanced phosphorescent materials for applications in visual display technologies, dynamic patterning, and information security.

Conclusions

In this study, we developed a regioselective synthetic strategy for the construction of 2,1-BN naphthalene derivatives using various *ortho*-halogenated phenylboronic acids, enabling the controlled synthesis of representative BN-fused isomers. The broad substrate compatibility underscores the generality and efficiency of this approach. Photophysical investigations revealed that both isomers exhibit RTP when embedded in a polyvinyl alcohol (PVA) matrix. Notably, the **3a@PVA** film demonstrated outstanding RTP performance, featuring an ultralong phosphorescence lifetime of 2388.2 ms and a visible afterglow lasting up to 30 seconds. This pronounced difference can be attributed to the presence of more efficient ISC channels, larger SOC values, and the more stable interactions between the **3a** molecule and the PVA matrix, which collectively endow the material with enhanced potential for anti-counterfeiting applications. Overall, this work not only offers an efficient and versatile synthetic route to structurally defined BN isomers but also establishes a robust, patternable RTP platform, laying a foundation for the functional development of BN-based phosphorescent materials.

Author contributions

Qiang Feng and Jianhua Liu conceptualized the project methodology, supervised the investigation, collected experimental data, built the data pipeline, analysed the data and wrote the original draft. Junxiong Yao collected experimental data, built the data pipeline and analysed the data. Yang Qiu, Zicheng Wang, Xia Wang, Weilin Chen, and Qianxin Wu collected experimental data and analysed the data. Xiaohua Cao, Jianqi Sun and Qianqian Ye built the data pipeline. Huanan Huang, Jianguo Wang and Dianyuan Wang conceptualized the project

methodology, supervised the investigation and co-wrote the manuscript.

Conflicts of interest

The authors declare no competing financial interest.

Data availability

All data supporting the findings of this study are provided in the main text and the SI.

The supplementary information (SI) for this article contains all relevant experimental details, including the synthesis procedures of the compounds, preparation methods of doping films, characterization data for the products, photoluminescence (PL) studies, density functional theory (DFT) calculations, and NMR spectroscopic data. See DOI: **https://doi.org/10.1039/d5sc05061h**.

Acknowledgements

This work was supported by the National Natural Science Foundation of China (No. 22261028, 22465022, and 22164012); the Jiangxi Province Outstanding Youth Fund (20202ACBL213003); the "Double-Thousand" Talent Plan; the Education Department of Jiangxi Province Foundation of China (No. GJJ2201905 and GJJ2401811).

Notes and references

1 P. G. Campbell, A. J. V. Marwitz and S.-Y. Liu, *Angew. Chem., Int. Ed.*, 2012, **51**, 6074–6092.
2 M. M. Morgan and W. E. Piers, *Dalton Trans.*, 2016, **45**, 5920–5924.
3 Z. X. Giustra and S.-Y. Liu, *J. Am. Chem. Soc.*, 2018, **140**, 1184–1194.
4 M. L. Xiaoyang Xu, C. Li and X. Liu, *Chin. J. Inorg. Chem.*, 2023, **43**, 1611–1644.
5 Q. Feng, Y. Zhou, H. Xu, J. Liu, Z. Wan, Y. Wang, P. Yang, S. Ye, Y. Zhang, X. Cao, D. Cao and H. Huang, *Chem. Soc. Rev.*, 2025, **54**, 5995–6061.
6 J.-Y. Wang and J. Pei, *Chin. Chem. Lett.*, 2016, **27**, 1139–1146.
7 P.-F. Zhang, J.-C. Zeng, F.-D. Zhuang, K.-X. Zhao, Z.-H. Sun, Z.-F. Yao, Y. Lu, X.-Y. Wang, J.-Y. Wang and J. Pei, *Angew. Chem., Int. Ed.*, 2021, **60**, 23313–23319.
8 Z.-G. Wu, Y. Xin, C. Lu, W. Huang, H. Xu, X. Liang, X. Cao, C. Li, D. Zhang, Y. Zhang and L. Duan, *Angew. Chem., Int. Ed.*, 2024, **63**, e202318742.
9 X.-Y. Wang, H.-R. Lin, T. Lei, D.-C. Yang, F.-D. Zhuang, J.-Y. Wang, S.-C. Yuan and J. Pei, *Angew. Chem., Int. Ed.*, 2013, **52**, 3117–3120.
10 X.-Y. Wang, F.-D. Zhuang, R.-B. Wang, X.-C. Wang, X.-Y. Cao, J.-Y. Wang and J. Pei, *J. Am. Chem. Soc.*, 2014, **136**, 3764–3767.
11 W. Li, C.-Z. Du, X.-Y. Chen, L. Fu, R.-R. Gao, Z.-F. Yao, J.-Y. Wang, W. Hu, J. Pei and X.-Y. Wang, *Angew. Chem., Int. Ed.*, 2022, **61**, e202201464.
12 G. Meng, H. Dai, T. Huang, J. Wei, J. Zhou, X. Li, X. Wang, X. Hong, C. Yin, X. Zeng, Y. Zhang, D. Yang, D. Ma, G. Li, D. Zhang and L. Duan, *Angew. Chem., Int. Ed.*, 2022, **61**, e202207293.
13 C. Li, Y. Sun, N. Xue, Y. Guo, R. Jiang, Y. Wang, Y. Liu, L. Jiang, X. Liu, Z. Wang and W. Jiang, *Angew. Chem., Int. Ed.*, 2025, **64**, e202423002.
14 H. Huang, Y. Zhou, M. Wang, J. Zhang, X. Cao, S. Wang, D. Cao and C. Cui, *Angew. Chem., Int. Ed.*, 2019, **58**, 10132–10137.
15 Y. Chen, W. Chen, Y. Qiao, X. Lu and G. Zhou, *Angew. Chem., Int. Ed.*, 2020, **59**, 7122–7130.
16 H. Huang, L. Liu, J. Wang, Y. Zhou, H. Hu, X. Ye, G. Liu, Z. Xu, H. Xu, W. Yang, Y. Wang, Y. Peng, P. Yang, J. Sun, P. Yan, X. Cao and B. Z. Tang, *Chem. Sci.*, 2022, **13**, 3129–3139.
17 H. Huang, J. Yao, H. Xu, J. Li, H. Wang, C. Xiong, B. Fang, Y. Wang, Y. Zhou, X. Cao, J. Wang and B. Z. Tang, *Adv. Opt. Mater.*, 2023, **11**, 2202433.
18 H. Xu, J. Yao, W. Tu, X. Zheng, H. Fu, Q. Xu, S. Zhang, J. Li, H. Wang, J. Fang, J. Yang, C. Xu, X. Cao and H. Huang, *Org. Chem. Front.*, 2023, **10**, 5352–5361.
19 J. Yao, Q. Meng, Q. Xu, H. Fu, H. Xu, Q. Feng, X. Cao, Y. Zhou, H. Huang, C. Bai and R. Qiao, *Talanta*, 2024, **280**, 126734.
20 C. Bai, J. Yao, Q. Meng, Y. Dong, M. Chen, X. Liu, X. Wang, R. Qiao, H. Huang, B. Wei, C. Qu and H. Miao, *J. Hazard. Mater.*, 2024, **469**, 133968.
21 F. J. R. Rombouts, F. Tovar, N. Austin, G. Tresadern and A. A. Trabanco, *J. Med. Chem.*, 2015, **58**, 9287–9295.
22 P. Zhao, D. O. Nettleton, R. G. Karki, F. J. Zécri and S.-Y. Liu, *ChemMedChem*, 2017, **12**, 358–361.
23 K. Boknevitz, J. S. Italia, B. Li, A. Chatterjee and S.-Y. Liu, *Chem. Sci.*, 2019, **10**, 4994–4998.
24 B. A. Haney, C. L. Schrank and W. M. Wuest, *Tetrahedron Lett.*, 2021, **62**, 152667.
25 M. J. S. Dewar, V. P. Kubba and R. Pettit, *J. Chem. Soc.*, 1958, 3073–3076.
26 M. J. S. Dewar and R. Dietz, *J. Chem. Soc.*, 1959, 2728–2730.
27 H. Huang, Z. Pan and C. Cui, *Chem. Commun.*, 2016, **52**, 4227–4230.
28 M. Chen, K. S. Unikela, R. Ramalakshmi, B. Li, C. Darrigan, A. Chrostowska and S.-Y. Liu, *Angew. Chem., Int. Ed.*, 2021, **60**, 1556–1560.
29 P. B. Pati, E. Jin, Y. Kim, Y. Kim, J. Mun, S. J. Kim, S. J. Kang, W. Choe, G. Lee, H.-J. Shin and Y. S. Park, *Angew. Chem., Int. Ed.*, 2020, **59**, 14891–14895.
30 X. Zhang, W. Su, H. Guo, P. Fang, K. Yang and Q. Song, *Angew. Chem., Int. Ed.*, 2024, **63**, e202318613.
31 H. Braunschweig, K. Geetharani, J. O. C. Jimenez-Halla and M. Schäfer, *Angew. Chem., Int. Ed.*, 2014, **53**, 3500–3504.
32 M. Schäfer, J. Schäfer, R. D. Dewhurst, W. C. Ewing, M. Krahfuß, M. W. Kuntze-Fechner, M. Wehner, C. Lambert and H. Braunschweig, *Chem.–Eur. J.*, 2016, **22**, 8603–8609.
33 M. Heß, I. Krummenacher, T. Dellermann and H. Braunschweig, *Chem.–Eur. J.*, 2021, **27**, 9503–9507.

34 D. Tian, G. Shi, M. Fan, X. Guo, Y. Yuan, S. Wu, J. Liu, J. Zhang, S. Xing and B. Zhu, *Org. Lett.*, 2021, **23**, 8163–8168.
35 Y. He, H. Wang, Y. Zhou, K. Yang and Q. Song, *Org. Chem. Front.*, 2023, **10**, 127–132.
36 T. Kaehler, M. Bolte, H.-W. Lerner and M. Wagner, *Angew. Chem., Int. Ed.*, 2019, **58**, 11379–11384.
37 O. Ouadoudi, T. Kaehler, M. Bolte, H.-W. Lerner and M. Wagner, *Chem. Sci.*, 2021, **12**, 5898–5909.
38 M. Tsuda, T. Morita and H. Nakamura, *Chem. Commun.*, 2022, **58**, 1942–1945.
39 H. Huang, Y. Zhou, Y. Wang, X. Cao, C. Han, G. Liu, Z. Xu, C. Zhan, H. Hu, Y. Peng, P. Yan and D. Cao, *J. Mater. Chem. A*, 2020, **8**, 22023–22031.
40 D. S. Surry and S. L. Buchwald, *Chem. Sci.*, 2011, **2**, 27–50.
41 S. Santoro, S. I. Kozhushkov, L. Ackermann and L. Vaccaro, *Green Chem.*, 2016, **18**, 3471–3493.
42 J. H. Docherty, T. M. Lister, G. McArthur, M. T. Findlay, P. Domingo-Legarda, J. Kenyon, S. Choudhary and I. Larrosa, *Chem. Rev.*, 2023, **123**, 7692–7760.
43 F. Fache, E. Schulz, M. L. Tommasino and M. Lemaire, *Chem. Rev.*, 2000, **100**, 2159–2232.
44 F. Chen, L. Zhao, X. Wang, Q. Yang, W. Li, H. Tian, S. Shao, L. Wang, X. Jing and F. Wang, *Sci. China:Chem.*, 2021, **64**, 547–551.
45 M. Li, W. Xie, X. Cai, X. Peng, K. Liu, Q. Gu, J. Zhou, W. Qiu, Z. Chen, Y. Gan and S.-J. Su, *Angew. Chem., Int. Ed.*, 2022, **61**, e202209343.
46 R. Wills, R. Shirke, H. Hrncir, J. M. Talbott, K. Sad, J. M. Spangle, A. D. Gracz and M. Raj, *Chem. Sci.*, 2024, **15**, 4763–4769.
47 Z. Tang and P. Zhou, *ChemPhysChem*, 2024, **25**, e202400503.
48 Y. Su, S. Z. F. Phua, Y. Li, X. Zhou, D. Jana, G. Liu, W. Q. Lim, W. K. Ong, C. Yang and Y. Zhao, *Sci. Adv.*, 2018, **4**, eaas9732.
49 X. Zhen, Y. Tao, Z. An, P. Chen, C. Xu, R. Chen, W. Huang and K. Pu, *Adv. Mater.*, 2017, **29**, 1606665.
50 X.-F. Wang, H. Xiao, P.-Z. Chen, Q.-Z. Yang, B. Chen, C.-H. Tung, Y.-Z. Chen and L.-Z. Wu, *J. Am. Chem. Soc.*, 2019, **141**, 5045–5050.
51 W.-L. Zhou, W. Lin, Y. Chen and Y. Liu, *Chem. Sci.*, 2022, **13**, 7976–7989.
52 H. Sun and L. Zhu, *Aggregate*, 2023, **4**, e253.
53 Y. Zhou, W. Qin, C. Du, H. Gao, F. Zhu and G. Liang, *Angew. Chem., Int. Ed.*, 2019, **58**, 12102–12106.
54 F. Guo, Y. Chen, C. Li, X. Wang, Q. Li, M. He, H. Hou and C. Yang, *Adv. Funct. Mater.*, 2025, **35**, 2416465.
55 R. Kabe, N. Notsuka, K. Yoshida and C. Adachi, *Adv. Mater.*, 2016, **28**, 655–660.
56 T. Wang, X. Su, X. Zhang, X. Nie, L. Huang, X. Zhang, X. Sun, Y. Luo and G. Zhang, *Adv. Mater.*, 2019, **31**, 1904273.
57 X. Ma, T.-J. Ye, H.-J. Yang, G.-K. Ling, D. Wang, J.-S. Li, P. Gu, L.-J. Xu, T.-L. Sheng, F.-R. Lin, R.-F. Shen and Q. Zhang, *Aggregate*, 2024, **5**, e579.
58 D. Li, Y. Yang, J. Yang, M. Fang, B. Z. Tang and Z. Li, *Nat. Commun.*, 2022, **13**, 347.
59 M. S. Kwon, D. Lee, S. Seo, J. Jung and J. Kim, *Angew. Chem., Int. Ed.*, 2014, **53**, 11177–11181.
60 W. Li, W. Zhou, Z. Zhou, H. Zhang, X. Zhang, J. Zhuang, Y. Liu, B. Lei and C. Hu, *Angew. Chem., Int. Ed.*, 2019, **58**, 7278–7283.
61 H. Zheng, P. Cao, Y. Wang, X. Lu and P. Wu, *Angew. Chem., Int. Ed.*, 2021, **60**, 9500–9506.
62 Y. Yao, D. Huang, P. Han, X. Peng, X. He, H. Xu, A. Qin and B. Z. Tang, *ACS Mater. Lett.*, 2025, **7**, 133–140.
63 J. Gong, L. Liu, C. Li, Y. He, J. Yu, Y. Zhang, L. Feng, G. Jiang, J. Wang and B. Z. Tang, *Chem. Sci.*, 2023, **14**, 4863–4871.
64 J. Liu, J. Yao, R. Mu, X. Mao, H. Li, J. Sun, J. Huang, Q. Feng, X. Cao, J. Wang and H. Huang, *Angew. Chem., Int. Ed.*, 2025, e202509104.